Thermo-mechanical characterization of steel-based metal matrix composite reinforced with TiB2 particles using synchrotron X-ray diffraction

M.S. Commisso, Christophe Le Bourlot, Bonnet Frédérique, O. Zanelatto, E. Maire

Thermo-mechanical characterization of steel-based metal matrix composite reinforced with TiB_2 particles using synchrotron X-ray diffraction

M.S. Commisso, C. Le Bourlot, F. Bonnet, O. Zanelatto, E. Maire

PII: S2589-1529(19)30107-3
DOI: https://doi.org/10.1016/j.mtla.2019.100311
Article Number: 100311
Reference: MTLA 100311

To appear in: *Materialia*

Received date: 24 October 2018
Revised date: 31 March 2019
Accepted date: 1 April 2019

Please cite this article as: M.S. Commisso, C. Le Bourlot, F. Bonnet, O. Zanelatto, E. Maire, Thermo-mechanical characterization of steel-based metal matrix composite reinforced with TiB_2 particles using synchrotron X-ray diffraction, *Materialia* (2019), doi: https://doi.org/10.1016/j.mtla.2019.100311

Thermo-mechanical characterization of steel-based metal matrix composite reinforced with TiB_2 particles using synchrotron X-ray diffraction

M.S. Commisso[a,b,*], C. Le Bourlot[b], F. Bonnet[c], O. Zanelatto[b], E. Maire[b]

[a] *ECAM Lyon, 40, Montée Saint-Barthélemy, 69321 Lyon, France*
[b] *INSA Lyon, Bat St Exupéry, 69621 Villeurbanne Cedex, Lyon, France*
[c] *ArcelorMittal Research, Voie Romaine-BP30320, 57283 Maizieres-les-Metz Cedex, France*

Abstract

The thermo-mechanical properties of a ferritic-steel-based metal matrix composite reinforced with titanium diboride (TiB_2) particles were studied using synchrotron X-ray diffraction. The samples were subjected to *in situ* heat treatment to investigate the effect of the mismatch in the coefficient of thermal expansion between the matrix and reinforcement. In addition, *in situ* tensile tests were performed to examine the load partitioning in the composite. Load transfer from the ferritic matrix to the TiB_2 particles was observed at the onset of plasticity in the matrix.

Keywords: `Metal matrix composite`, `Steel-based composite`, `X-ray diffraction`

1. Introduction

Metal matrix composites (MMCs) consist of a ductile metal or alloy matrix embedded with rigid ceramic reinforcements. These materials combine the ductility and toughness of metals with the high strength and modulus of ceramics, leading to improved shear and compression strengths and higher service-temperature capabilities compared with those of unreinforced alloys [1]. In addition, the high specific modulus of MMCs is advantageous for applications requir-

*Corresponding author
Email address: `m.commisso@ecam.fr` (M.S. Commisso)

ing further weight reduction. These properties of MMCs make them promising candidates for aerospace, automotive, and other structural applications.

Aluminium-based MMCs have been intensively studied because of the inherently low density of the aluminium matrix [2, 3, 4]. However, steel-based MMCs, also termed high-modulus steels (HMSs), are also particularly attractive. In addition to possessing a specific modulus comparable to that of e.g. aluminium (approximately 25 GPa.g.cm^{-3}), steel-based MMCs also exhibit a wide variety of mechanical properties owing to their multiple equilibrium phase transformations, have low production costs, and are easily recyclable [5]. These materials exhibit higher elastic moduli and improved wear resistance compared with those of unreinforced alloys [6]. Furthermore, as steel exhibits high toughness, the reduction in toughness of MMCs compared with that of unreinforced alloys, is less critical than in some aluminium-based MMCs. Another advantage of steel-based MMCs is the lower density of the ceramic reinforcements, such as TiB_2, relative to that of iron; the addition of these reinforcements thus reduces the density of the final material while also increasing its stiffness. In addition, the existence of a eutectic point in the Fe-TiB_2 phase diagram indicates the possibility of producing these MMCs using an industrial process such as continuous casting [7]. TiB_2 particles have also received considerable attention for HMS design because they can form a strong interface with steel matrices [8]. Steel-based MMCs are thus receiving increasing attention for numerous applications. ArcelorMittal has recently designed a family of steel composites using *in situ* precipitation of ceramic particles during eutectic solidification [9].

The objective of the current study was to characterize the thermal and mechanical behaviour of a ferritic steel reinforced with TiB_2 particles produced by ArcelorMittal. *In situ* thermal treatment and tensile tests were performed in an X-ray diffractometer to study the interaction between the ceramic particles and ferritic matrix.

2. Materials and Methods

A ferritic-steel-based composite reinforced with $10-15\%$ volume fraction of TiB_2 particles was provided by Arcelor-Mittal Research SA. The ceramic TiB_2 particles were produced by *in situ* precipitation during eutectic solidification.

Synchrotron X-ray diffraction (XRD) measurements were performed at beamline ID15B at the European Synchrotron Radiation Facility (ESRF) (Grenoble). The specimen was irradiated by a beam of 80-keV photons (corresponding to a wavelength of $\lambda = 1.55\text{x}10^{-11}m$). A reference powder sample (CeO_2, ceria) was used to calibrate the diffraction peak positions. The diffraction pattern was recorded using a 16-bit charge-coupled device (CCD) camera with a 154 x 154 pixel sensor. The camera was positioned ≈0.9 m from the specimen. This set-up allowed 360° of the diffraction rings to be recorded, enabling different strain directions to be measured. Figure 1 shows the diffraction rings for the TiB_2 powder (Figure 1a) and composite (Figure 1b) at room temperature.

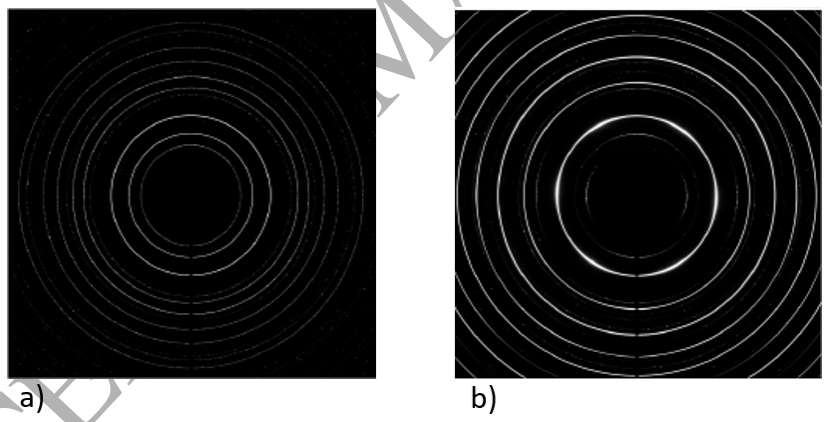

Figure 1: Diffraction rings for a) TiB_2 powder and b) composite at room temperature.

Each CCD image was then "caked", which means that the intensity data was integrated over a certain angle to produce a mean diffraction pattern from the segment of the diffraction rings recorded in the CCD image. Very sharp diffraction peaks were obtained because of the high resolution of the CCD.

To avoid calibration errors, even when a calibration sample was used, all the results were calculated using the diameter of the ring instead of the radius, thereby avoiding errors resulting from miscalculations of the centre position. Furthermore, the statistics of the values are improved when using the diameter of the ring (these calculations are called 4θ calculations).

The 2D CCD images were then reduced into 1D curves (2θ vs. intensity) by azimuthal integration using the open-source software pyFAI (Fast Azimuthal Integration in Python); see [10] for further details. The integration of the rings was performed at different angles to evaluate the strains in different directions. The amplitude around the integration angle was varied to determine its effect, and different windows were used: $\pm 10°, 15°$ and $20°$. The integration window did not have a remarkable effect on the resulting lattice constants; therefore, a window of $\pm 15°$ was selected.

The lattice spacing, d, was estimated using Bragg's law:

$$2d \sin\theta = \lambda. \tag{1}$$

Finally, diffraction patterns in the longitudinal and transverse directions were obtained by integration around 0° and 90°, respectively.

2.1. In situ thermal treatment in X-ray diffractometer

In situ thermal treatment of the composite and ceramic component was performed in the X-ray diffractometer. A bar sample of the composite was continuously heated (0.3°C/s) until reaching 1080°C, held at the maximum temperature for 25 min, and then cooled down at the same rate as that used for heating. The same treatment was used for a powder sample of TiB_2 obtained by dissolution of the matrix in the composite. Using this thermal treatment, a diffraction curve was obtained every 3° to 5°C.

2.2. In situ tensile tests in X-ray diffractometer

To evaluate the load partitioning, *in situ* tensile tests were performed in the X-ray diffractometer using dog-bone-shaped specimens. Displacement-controlled

tests were performed. The strain was estimated from optical images of the patterned (painted) surface of the sample obtained during the tensile test using the image correlation technique.

3. Results

3.1. Phase identification

As the composite was initially hot rolled, a microstructure highly oriented in the rolling direction was obtained. Figure 2 presents a typical scanning electron microscopy (SEM) backscattered electron (BSE) image of the studied samples. The microstructure consisted of primary TiB_2 crystals surrounded by a eutectic mixture of ferrite and smaller TiB_2 particles. The large and prismatic particles (10–20 μm) are the primary TiB_2 crystals, and the small and elongated particles were formed during the eutectic reaction (1–10 μm). Both types of particles were uniformly distributed in the sample.

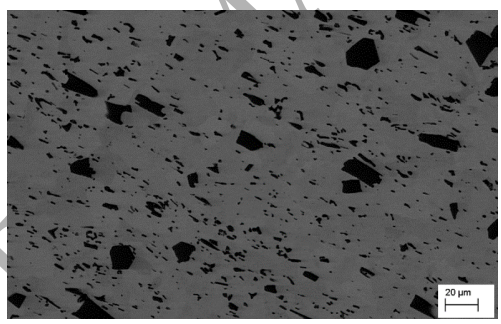

Figure 2: Representative BSE image of MMC.

The peaks of the XRD patterns of the powder sample indicate that the TiB_2 particles exhibited a hexagonal crystal structure. The phases and crystal planes are identified in Figure 3a). Traces of TiC were detected in the powder sample, indicating that TiC particles were likely located in the boundary between the steel and TiB_2 particles, as previously reported in [11, 12].

The refined values of the lattice parameters were obtained by performing single-peak analysis (see Figure 4b). Using this type of analysis, it is possible

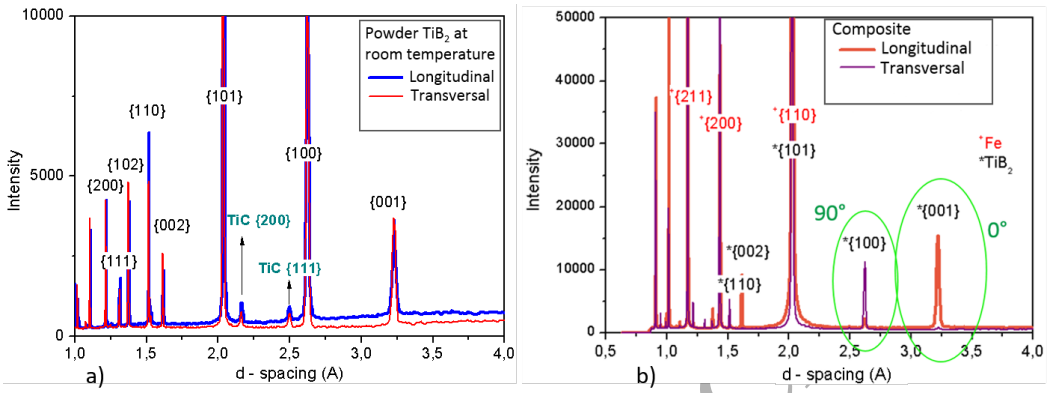

Figure 3: Diffraction pattern at room temperature for a) TiB_2 powder and b) composite in longitudinal (integrated around 0°) and transverse direction (integrated around 90°).

to find the centre position of the peak at each temperature: μ_1. The centre position of the peak can then be used to define the lattice parameter using the following expression for a hexagonal lattice structure:

$$\frac{1}{d^2} = \left(\frac{4}{3}\right)\frac{h^2 + hk + k^2}{a^2} + \frac{l^2}{c^2}. \tag{2}$$

(3)

Using the positions of the {100} and {001} planes in the powder sample, the following expressions were obtained for the lattice parameters: $a = \frac{2}{\sqrt{3}\mu_1}$ and $c = \frac{1}{\mu_1}$; therefore, values of

$$a = 3.0315\mathring{A}, \tag{4}$$

$$c = 3.2307\mathring{A}, \tag{5}$$

were determined at room temperature. The anisotropy of the crystal was determined using these estimated values; a ratio of $c/a = 1.066$ was obtained, which is the same value determined by [13, 14] for monocrystals of TiB_2 at room temperature. These lattice parameters can be considered the values for the "stress-free" state.

As reported by [14], the processing conditions significantly affect the physical, mechanical, and thermal properties of TiB_2. Therefore, it was critical to characterize the properties of the TiB_2 in the studied MMC.

The texture of a sample is the distribution of its crystallographic orientation, and the relation between the intensity of the peaks for different hkl planes can be related to the texture present in a crystal structure. This relation can be used to describe the crystal orientation in the composite sample. As observed in Figure 1, the brightness of the rings in the composite was not uniform along the perimeter of the ring, indicating an anisotropic texture. This finding was corroborated by the azimuthal integration, which resulted in plane peaks only in the preferred orientation (the direction in which the crystal plane was oriented). In addition to the TiB_2 particles in the composite being macroscopically oriented in the rolling direction (shape orientation), the crystals were also oriented in a specific way. The {001} plane was only visible when the azimuthal integration around 0° was performed. This plane corresponds to the c or basal direction of the hexagonal crystal cell and was oriented in the longitudinal direction, i.e., the rolling direction. In contrast, the a axis of the crystal structure was visible for the integration around 90°, indicating that the a axis was oriented perpendicular to the rolling direction. This feature is clearly observed in the highlighted oval areas in Figure 3b). For the ferrite, there were no remarkable differences in its behaviour in the longitudinal and transverse directions.

3.2. Heat treatment results

The procedure used to determine the peak positions at different temperatures is summarized in Figure 4. Figure 4a) presents the full diffraction patterns for selected curves as a function of temperature, and the analysis of a single peak position is shown in Figure 4b).

The analysis of single peaks during the heat treatment was used to determine the variation of the lattice parameters with temperature of these TiB_2 particles in their stress-free state. The lattice parameters clearly increased with increasing temperature in a linear manner (as observed in Figure 5).

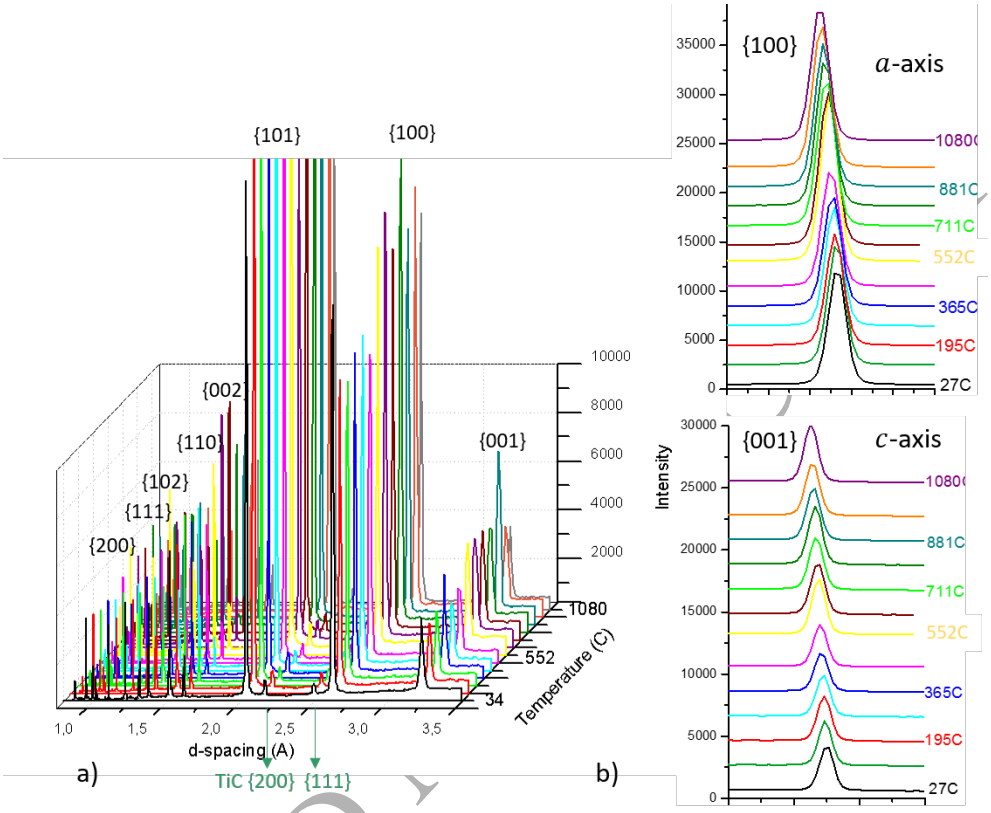

Figure 4: a) XRD patterns of TiB_2 powder showing the evolution of the transformation with the temperature. b) Single-peak analysis for $a-$axis (top) and $c-$axis (bottom). Only selected curves are shown.

The thermal expansion coefficient for TiB_2 was extracted from the slope of the linear relation. The linear thermal expansion coefficient, α, was calculated along the $a-$ and $c-$axis using the following equations:

$$\alpha_a = \frac{1}{a_0}\left(\frac{a}{\Delta T}\right) \qquad \alpha_c = \frac{1}{c_0}\left(\frac{c}{\Delta T}\right), \tag{6}$$

where a and T denote the unit-cell axis and temperature, respectively, and a_0 and c_0 are the lattice parameters at room temperature estimated using equations

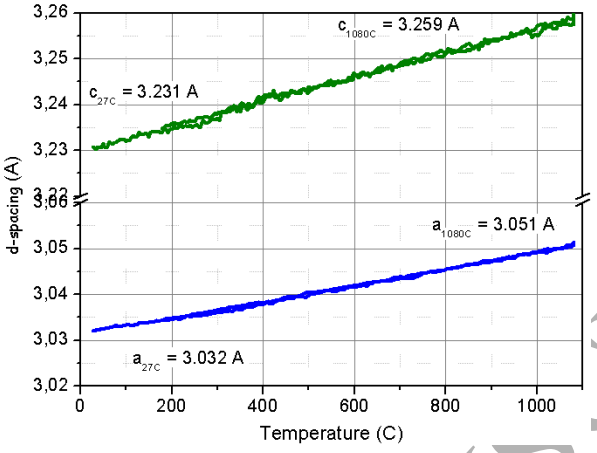

Figure 5: Variation of lattice parameters of hexagonal crystal structure of TiB_2 with temperature.

(4) and (5), respectively, resulting in

$$\alpha_a = 5.92.10^{-6}\, 1/K, \tag{7}$$

$$\alpha_c = 8.47.10^{-6}\, 1/K. \tag{8}$$

The anisotropy of the thermal expansion was calculated to be $\alpha_c/\alpha_a = 1.43$. This value was compared with the α estimated by [13] for monocrystals. In that study, a differential dilatometer was used to calculate the coefficient of thermal expansion. The authors obtained values of $\alpha_a = 6.35.10^{-6}\, 1/K$ and $\alpha_c = 9.30.10^{-6}\, 1/K$, which led to an anisotropy ratio of $\alpha_c/\alpha_a = 1.46$, which corresponds well with our current results. We can also appreciate that the variation of the coefficient of thermal expansion with temperature was rather small, as mentioned in [13], as we obtained a good linear regression for the relation of the lattice parameters over the entire temperature range.

The evolution of the lattice parameters of the TiB_2 in the composite was subsequently analysed by heating and cooling one of the composite samples. The results are compared with those obtained for the powder sample in Figure 6.

The strong texture present in the composite induced a very weak intensity

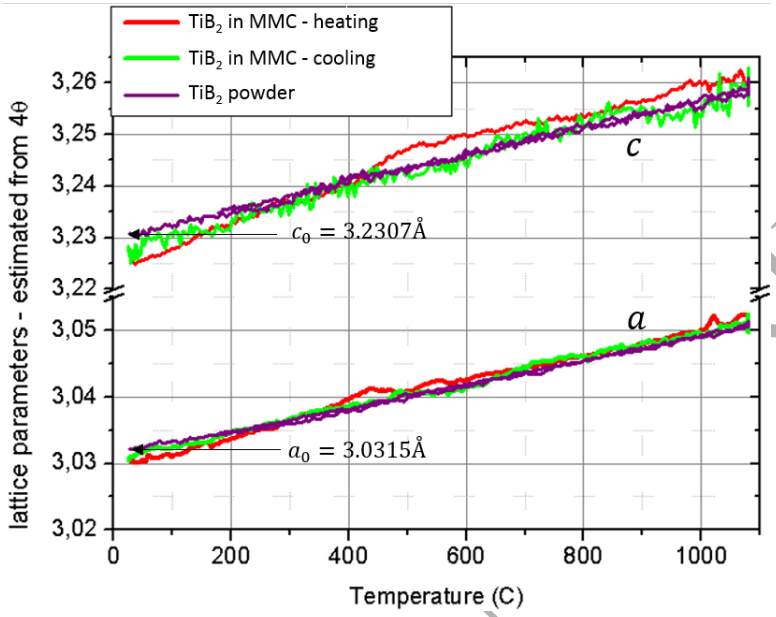

Figure 6: Variation of the lattice parameters of TiB_2 in the composite with temperature.

of the TiB_2 reflection in certain directions. Thus, we were only able to estimate the parameters c and a when integrating around the longitudinal and transverse axis, respectively. The initial lattice parameter of the TiB_2 particles was smaller than that of the stress-free TiB_2, which indicates that the TiB_2 in the composite was initially subjected to compression. This is a quite classical observation in MMCs [4, 11, 15] and can be explained by the greater dilation of the metal matrix than of the ceramic phase during cooling from the fabrication temperature. Upon increasing the temperature, the lattice constants increased; however, the slope was higher than for the stress-free particles as Fe expands faster than TiB_2, which relieves the initial internal stresses. At approximately $300 - 400°C$, the initial thermal internal stresses were completely relieved. At that point, a and c continued to linearly increase and reached values that were even higher than those estimated for the powder. This result implies that the TiB_2 particles were subjected to tensile strains, and thus, the matrix must be pulling the reinforcement. This finding suggests that the composites exhibit

very good interfacial adhesion. The linear (and thus elastic) increase of strain in the particles stopped at approximately 500°C, likely because Fe started to plastify or creep at these high temperatures. During the 25-min holding at 1080°C, the strain in the TiB_2 completely relaxed because of the creep process, and the particles were close to stress-free before cooling. During the beginning of the cooling process, no strain was built up in the particles, as indicated by the similarity of the cooling curves for the composite and stress-free particles. At 500°C, the matrix stopped creeping, and the slope of the curve for the composite changed and deviated from that of the stress-free particles such that at the end of the thermal cycle, the thermal internal strain was similar to that at the beginning. At $900 - 1000$°C small unstable fluctuations in the strain were observed, which we attribute to the phase transformation of iron from ferrite to austenite.

In Figure 7, the lattice parameter of the ferrite is shown as a function of temperature in the longitudinal and transverse directions. No noticeable differences were observed between the two directions. However, fluctuations in the lattice parameter were observed for temperatures near $900 - 1000$°C, possibly resulting from the ferrite-to-austenite transformation.

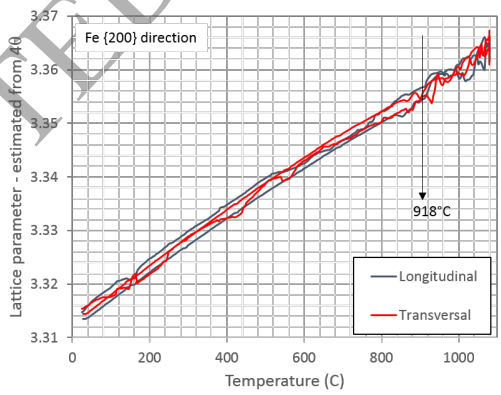

Figure 7: Variation of lattice parameter of Fe with temperature in longitudinal and transverse directions, calculated using the {200} peak.

This ferrite-to-austenite transformation can be clearly observed in the XRD

pattern in Figure 8. If we analyse the {110} peak of Fe, we can see that at room temperature, a single peak of ferrite is present; however, upon increasing the temperature, the amount of the austenite phase increases, and therefore, the austenite peaks can also be distinguished in the spectra. The austenite phase becomes visible at approximately 918°C.

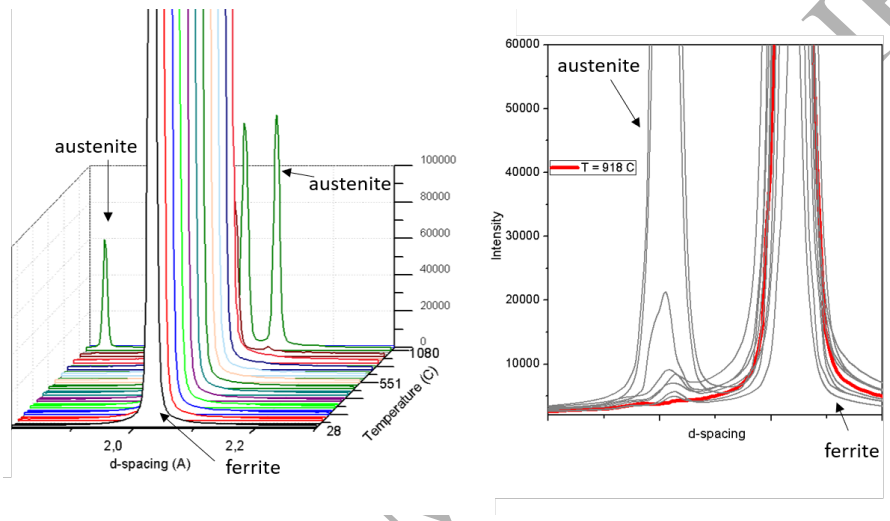

Figure 8: XRD patterns of iron reflections. The analysis of {110} peak allows the identification of the ferrite-to-austenite transformation. At the right, the image shows the austenite phase appearance, which becomes visible at approximately 918°C where new peaks can be distinguished.

3.3. Tensile test results

A composite sample was loaded in tension in the longitudinal (rolling) direction. To analyse the load partitioning in the material, the lattice strains for the particles and matrix were calculated. The initial residual stress of the TiB_2 was calculated using the lattice parameters of the powder sample as a reference. The strain is given by

$$\epsilon_a = \frac{a - a_0}{a_0}, \tag{9}$$

where ϵ_a represents the strain in the lattice a direction, a is the lattice parameter obtained from the centre position of the diffraction peak, and a_0 is the reference value obtained using equation (4). An analogous relationship can be expressed for the c direction.

For the Fe phase, the lattice parameter at the beginning of the test was used as a reference because the stress-free state was not available, which leads us to assume that the residual thermal strain was negligible in the Fe phase of the composite. This assumption is considered a reasonable approximation. The lattice parameters obtained in the longitudinal and transverse directions were similar; nevertheless, two different curves using their respective reference parameters were calculated.

The initial strains for the particles and matrix are summarized in Table 1.

Table 1: Initial residual strains for TiB_2 and ferrite in longitudinal and transverse directions.

TiB_2				Fe			
a_0 (Å)	ϵ_a	c_0 (Å)	ϵ_c	a_{0long} (Å)	ϵ_l	a_{0trans} (Å)	ϵ_t
3.0315	$-6.3.10^{-4}$	3.2307	$-1.64.10^{-3}$	3.3138	0	3.3134	0

The internal strains for TiB_2 and ferrite were calculated from XRD patterns obtained at different times during the tensile test.

In Figure 9, the macroscopic or applied stress is presented as a function of the internal strain in each phase (Fe and TiB_2). The responses in the longitudinal and transverse directions can be seen.

A linear response for the iron reflection up to an applied stress of 410 MPa is observed in Figure 9a) (limit marked with a solid line). Beyond this stress level, there was a change in the slope in the curve. The curve turned upward, which indicates that the relative stress carried by the matrix was reduced while the macroscopic stress was increased. This change in the slope may result from the onset of plasticity in the matrix, which would, in turn, increase the elastic mismatch with the particles that deform only elastically. The matrix is the

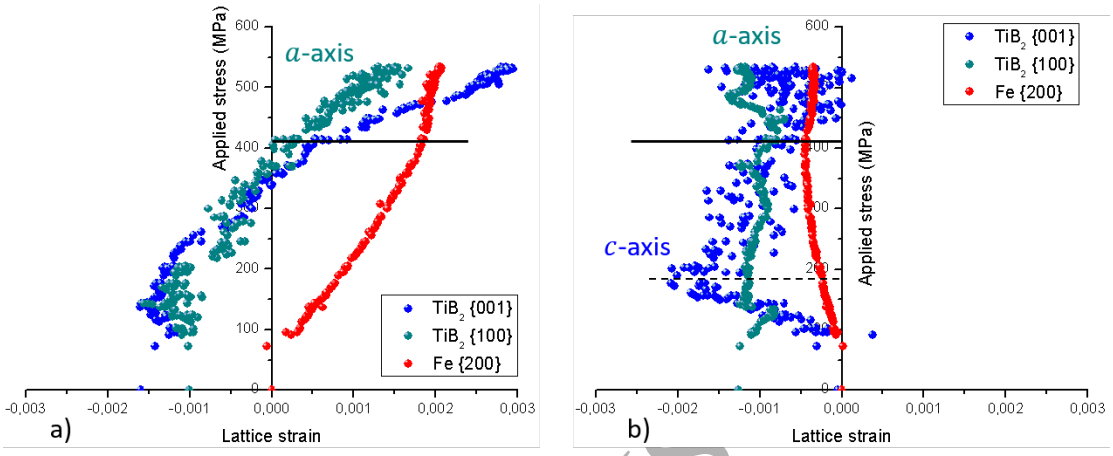

Figure 9: Tensile responses of composite in a) longitudinal and b) transverse directions.

less stiff phase of the material, and because it deforms plastically, the degree of mismatch is even higher, leading to an increase in the load transfer to the reinforcement. It can also be observed that the lattice strain estimated in the c direction was higher than that estimated in the a direction for the same applied stress. This finding can be attributed to two characteristics of the material: the texture in the samples, with the c-axis oriented in the tensile direction, and the anisotropy in the elastic properties in the TiB_2 particles. The basal (c) plane possessed a lower elastic modulus (approximately 430 GPa) than that in the a-direction (approximately 630 MPa) (see [13]).

Regarding the transverse response, the lattice strain of the iron phase linearly increased (in absolute value) owing to Poisson's contraction until the onset of plasticity in the matrix (see Figure 9b) up to the solid line). In contrast, three different regions were identified for the lattice strain of the reinforcement. During the initial period, the transverse strain increased in negative value owing to Poisson's contraction, as marked by the dashed line in Figure 9b). During the second period, close to reaching the onset of plasticity in the matrix, the lattice strain tended towards positive values of strains. This effect can be attributed to an increase in the effective bulk Poisson's ratio of the steel from 0.33 to 0.5 re-

sulting from conservation of volume upon plasticity. Finally, in the last period, the matrix exhibited plastic behaviour. During this last period, the strain in the particles increased more slowly than during the elastic loading. It still continued to slightly increase though because of the strain hardening of the matrix. This behaviour is similar to that observed in [15], where the authors examined the onset of plasticity in a 316L matrix and how it increased the mismatch with the TiB_2 particles, leading to load partitioning. Another interesting remark is that, as observed in the longitudinal direction, higher negative strains were also observed in the basal plane in the transverse direction because of its lower stiffness.

Because of the strong texture of the material, it was not simple to estimate the lattice strain of the basal plane (c) in the transverse direction (because the basal plane was oriented preferentially in the longitudinal direction), and the same issue occurred for the a direction in the longitudinal direction.

In a homogeneous and isotropic material, Hooke's law is defined as

$$\sigma = 2\mu\epsilon + \lambda \operatorname{tr}(\epsilon) I, \tag{10}$$

where I is the identity matrix, $\operatorname{tr}(\epsilon)$ is the trace of the deformation tensor, and μ and λ are Lamé constants defined as $\mu = E/[2(1+\nu)]$ and $\lambda = E\nu/[(1+\nu)(1-2\nu)]$. The internal stresses can be estimated assuming $\epsilon_2 = \epsilon_3$ and using the elastic constants obtained from the literature [13]: $E_a = 631.2$ GPa, $E_c = 427.2$ GPa, $\nu_a = 0.06$, and $\nu_c = 0.14$ and $E = 210$ GPa and $\nu = 0.33$ for the iron phase. Figure 10 shows the calculated internal stresses for the reinforcement and matrix as a function of the applied stress in the longitudinal direction.

The curves show that load transfer from the matrix to the reinforcement occurred in the elastic regime between $150 and 200$ MPa, which is consistent with the results presented in [15]. After the onset of plasticity in the matrix, the internal stresses of the reinforcement greatly increase, and there are only slight changes in the internal stresses in the iron phase. At higher stress, the slight change of the slope of the evolution of the stresses in the particles could be a signature of the beginning of the occurrence of damage (as observed, for

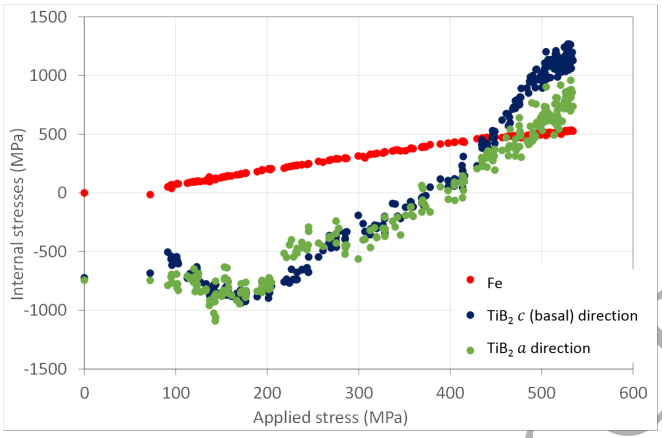

Figure 10: Tensile response of the composite in the longitudinal direction.

instance, in [16]), leading on average to stress relaxation in the TiB_2.

4. Conclusions

XRD was used to characterize a steel-based MMC. The composite was produced by precipitation of ceramic particles during eutectic transformation. SEM micrographs revealed that the reinforcement was oriented in the lamination direction, and XRD analysis revealed a strong texture. The TiB_2 had a hexagonal crystal structure; the basal (c) plane was preferentially oriented in the lamination direction, and the (a) plane was oriented in the transverse direction.

In situ thermal treatment of a powder sample of TiB_2 was performed, which enabled the thermal properties of the reinforcement to be estimated and a reference (stress-free) lattice parameter to be obtained. A linear relation between the lattice parameters and temperature was observed; it was thus possible to calculate a linear coefficient of thermal expansion. High anisotropy in the thermal properties was observed between the (a) and (c) directions, with a higher coefficient in the basal direction. A ratio of $\alpha_c/\alpha_a = 1.43$ was estimated, which corresponds well with previously reported values in the literature.

Thermal treatment of a composite sample was performed to analyse the effect of the mismatch in the coefficients of thermal expansion between the matrix and

reinforcement. The reinforcement was determined to initially be in compression, with higher levels of strain in the basal (c) direction. Upon increasing the temperature, the lattice constants for the TiB_2 in the composite increased with a higher slope than that observed in the powder sample because of the higher coefficient of thermal expansion of Fe. At approximately $300-400°C$, the initial thermal internal stresses were completely released. The linear increase of strain in the particles was observed until approximately 500°C, at which point Fe must have begun to plastify; thus, its effect on the lattice parameters of TiB_2 was reduced. After this point, a and c in the composite were larger than those calculated for the powder, which indicates that the TiB_2 was being pulled by the matrix, which can only occur if there is good interfacial cohesion between the two materials.

The austenitic transformation was identified using single-peak analysis. The autenite was estimated to appear at 918°C.

The initial stress state was estimated by assuming that the lattice parameters of the TiB_2 powder sample were those of the stress-free state. The *in situ* tensile tests enabled observation of the load partitioning in the composites. An initial transfer of load from the ferritic matrix to the reinforcement was observed in the earlier stages of plasticity of the matrix. This load transfer was identified by the change in the trend of the internal strains and stresses of each phase. A reduction in the slope in the ferrite phase was clearly observed in the composite. Subsequently, the stress carried by the reinforcement was reduced, which may have resulted from: 1. particle fracture (as identified in [16]), 2. particle/matrix interfacial fracture, and 3. the plastic yield of the matrix not increasing the stress substantially during deformation (thus, the load increase in the reinforcement was not significant). In general, higher internal strain was observed in the basal plane, likely because of the higher stiffness in this direction in the hexagonal structure of TiB_2.

5. Acknowledgements

This research was supported by Arcelor-Mittal Research SA. The authors would also like to thank Thomas Buslaps for assistance with the experiments at beamline ID15B at the European Synchrotron Radiation Facility (ESRF).

6. Conflict of interest statement

The authors declare that there is no conflict of interest.

References

References

[1] S. Tjong, Z. Ma, Microstructural and mechanical characteristics of in situ metal matrix composites, Materials Science and Engineering 29 (2000) 49–113.

[2] S. Jayalakshmi, S. Gupta, S. Sankaranarayanan, S. Sahu, M. Gupta, Structural and mechanical properties of Ni60Nb40 amorphous alloy particle reinforced Al-based composites produced by microwave-assisted rapid sintering, Materials Science and Engineering: A 581 (2013) 119 – 127.

[3] F. Chen, Z. Chen, F. Mao, T. Wang, Z. Cao, TiB_2 reinforced aluminum based in situ composites fabricated by stir casting, Materials Science and Engineering: A 625 (2015) 357 – 368.

[4] S. Sajjadi, H.R.Ezatpour, M. T. Parizi, Comparison of microstructure and mechanical properties of A356 aluminum alloy/Al_2O_3 composites fabricated by stir and compo-casting processes, Materials & Design 34 (2012) 106 – 111.

[5] G. Krauss, Steels: Processing, Structure and Performance, ASM International, 2005.

[6] A. Anal, T. Bandyopadhyay, K. Das, Synthesis and characterization of TiB_2 reinforced iron based composites, Journal of Materials Processing Technology 172 (2006) 70–76.

[7] K. Tanaka, T. Saito, Phase equilibria in TiB_2-reinforced high modulus steel, Basic and Applied Research 20 (3) (1998) 207–214.

[8] R. Aparicio-Fernández, H. Springer, A. Szeczepaniak, H. Zhang, D. Raabe, In-situ metal matrix composite steels: Effect of alloying and annealing on morphology, structure and mechanical properties of TiB_2 particle containing high modulus steels, Acta Materialia 107 (2016) 38–48.

[9] A. R. group, Patent EP 1 897 963 A1, bulletin 2008/11 (2008).

[10] J. Kieffer, G. Ashiotis, PyFAI: a python library for high performance azimuthal integration on gpu, Proceedings of the 7th European Conference on Python in Science (EUROPSCIPY).

[11] L. Cha, S. Lartigue-Korinek, M. Walls, L. Mazerolles, Interface structure and chemistry in a novel steel-based composite $Fe - TiB_2$ obtained by eutectic solidification, Acta Materialia 60 (2012) 6382–6389.

[12] S. Lartigue-Korinek, M. Walls, N. Haneche, L. Cha, L. Mazerolles, F. Bonnet, Interfaces and defects in a successfully hot-rolled steel-based composite $FeTiB_2$, Acta Materialia 98 (2015) 297 – 305.

[13] N. Okamoto, M. Kusakari, K. Tanaka, H. Inui, S. Otani, Anisotropic elastic constants and thermal expansivities in monocrystal CrB_2, TiB_2, and ZrB_2, Acta Materialia 58 (2010) 76–84.

[14] R. Munro, Material properties of titanium diboride, Journal of Research of the National Institute of Standards and Technology 105 (2000) 709–720.

[15] D. Bacon, L. Edwards, J. Moffatt, M. Fitzpatrick, Synchrotron x-ray diffraction measurements of internal stresses during loading of steel-based

metal matrix composites reinforced with TiB_2 particles, Acta Materialia 59 (9) (2011) 3373–3383.

[16] Z. Hadjem-Hamouche, J.-P. Chevalier, Y. Cui, F. Bonnet, Deformation behavior and damage evaluation in a new titanium diboride (TiB_2) steel-based composite, Steel Research International 83 (6) (2012) 538 – 545.